

# Electrical Design Optimization of Single-Mode Tunnel-Junction-Based Long-Wavelength VCSELs

Manish Mehta, Danny Feezell, David A. Buell, Andrew W. Jackson, Larry A. Coldren, *Fellow, IEEE*, and John E. Bowers, *Fellow, IEEE*

**Abstract**—We present principles for tunnel-junction (TJ) design optimization for use in intracavity contacted long-wavelength vertical-cavity surface-emitting lasers (LW-VCSELs). Using the WKB approximation, we find that layer thicknesses of 10 nm on the n++ side and 10 nm on the p++ side are large enough to maximize quantum tunneling probability and small enough to yield low optical free-carrier absorption loss. We also conjecture that our experimental test structures and actual devices have far lower active acceptor concentration than we expect based on an analytical model. Finally, we calculate the necessary doping levels to enable single-mode operation of LW-VCSELs and incorporate these conditions into a complete optimized model of our VCSELs. Based on optimal  $I$ - $V$  curves, we can expect an increase in single-mode output power from 2 to 3.5 mW.

**Index Terms**—AllnAs, AllnGaAs, current spreading, InP, long-wavelength, tunnel diode, tunnel junction, vertical-cavity surface-emitting laser (VCSEL).

## I. INTRODUCTION

TUNNEL junctions (TJ) have found widespread application in high-frequency oscillators and thermophotovoltaic devices since their discovery in 1958 [1]–[3]. More recently, groups have incorporated TJ structures into long-wavelength vertical-cavity surface-emitting lasers (LW-VCSELs) in order to realize reduced optical loss, as well as current and optical confinement. LW-VCSELs offer a low-cost alternative to their in-plane counterparts in the access and metro-area network component market, but performance of these devices has been historically limited by the high resistance and excessive optical loss associated with high acceptor doping levels in the p-type distributed Bragg reflector (DBR) and current spreading layers [4]. In the last several years, groups incorporating TJ structures in LW-VCSELs have demonstrated multimode (MM) output power in excess of 9 mW and single-mode (SM) output power greater than 2.5 mW at 20 °C and 1.5 mW at 70 °C [5]–[9]. Several groups have also reported 3.125-Gb/s SM transmission up to 70 °C [8], [10]. Several other groups have also developed LW-VCSEL structures incorporating TJ layers which are lattice-matched to InP [11], [12].

While groups have presented work on the theoretical modeling and design principles of InGaAs and InGaAsN TJs on GaAs substrates [13], little has been made public about the modeling and design of AllnAs–InP and AllnGaAs–AllnGaAs TJs developed on InP. Moreover, little work has been presented on

TJ design for SM applications. The conventional wisdom on TJ growth has been to impress a maximum flux of carbon (C) atoms on a Hall calibration sample of the p++ layer and rely on the measured hole concentration to serve as the experimental limit. Unfortunately, this technique does not provide the most accurate or steadfast TJ design method for several reasons. First, the accuracy of the doping calibration is questionable since the actual Alln(Ga)As p++ layer thickness (10 nm) is only  $\sim 1\%$  of the prepared Hall sample thickness (1  $\mu\text{m}$ ). Second, the amphoteric nature of C in Alln(Ga)As can yield compensation effects reducing the overall hole concentration in the TJ [14]. Finally, since most of the aforementioned groups use an intracavity contact scheme to bypass current conduction through the DBRs, it is necessary that the TJ provides enough lateral spreading resistance to uniformly pump the active region. Designs that fail to take this into account tend to produce MM devices which are not suitable for applications requiring signal propagation longer than several hundreds of meters.

The aim of this paper is to model optimal TJ operation for use in SM LW-VCSELs and incorporate the modeled TJ characteristics with an optimized electrical design for the remainder of the device in order to determine the maximum SM output power for our current structure. In Section II, we present theoretical TJ characteristics based on a model developed by Demassa and Knott [15] and compare modeled TJ characteristics to experimental results. In Section III, we derive the TJ resistivities required for uniform current spreading and SM VCSEL operation over a range of aperture sizes. We proceed to use the model from Section II to determine the TJ doping densities required to achieve these desired resistivities. Since the electrical properties of the TJ are then optimized, Section IV examines physical layer thickness design of the TJ using tunneling probability metrics. We compare the optical loss in the experimental structure and the optimized physical design and quantify the effect of growth aberrations on the optical loss. Section V incorporates the results of the TJ optimization in the previous sections with active region diode characteristics, spreading resistance, heterobarrier voltage, and transport resistances to generate a complete  $I$ - $V$  model for the VCSEL. We present two calculated curves—one which closely matches our experimental  $I$ - $V$  results and the other which presents a theoretical  $I$ - $V$  curve for an optimal device. While some reduction in device voltage arises from changes in device geometry and cavity-length reduction, most of the improvement stems from the TJ optimization presented in earlier sections. Finally, we present the theoretical increase in SM output power and roll-off current associated with optimizing the electrical characteristics of the device.

Manuscript received February 1, 2006; revised March 23, 2006.

The authors are with the Department of Electrical and Computer Engineering, University of California Santa Barbara, Santa Barbara, CA 93106-9560 USA (e-mail: manish@ece.ucsb.edu).

Digital Object Identifier 10.1109/JQE.2006.876713

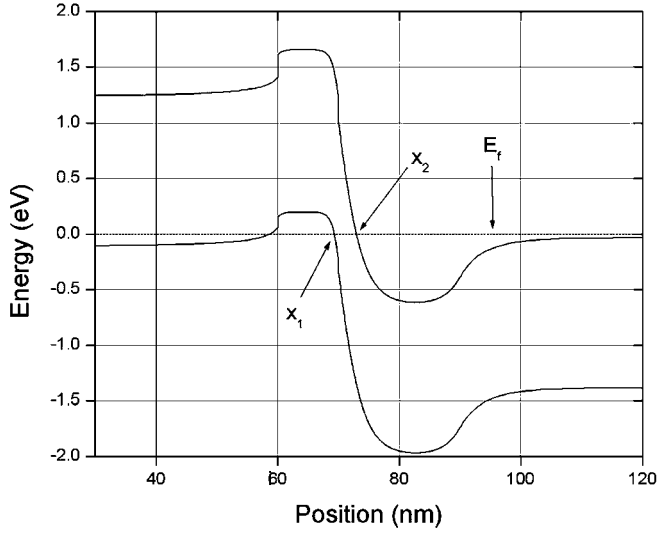


Fig. 1. Band diagram for an p++-AlInAs/n+-InP TJ doped  $2 \times 10^{20} \text{ cm}^{-3}$  and  $5 \times 10^{19} \text{ cm}^{-3}$  on the p and n sides, respectively. The points  $x_1$  and  $x_2$  represent the tunneling width limits at the Fermi level at equilibrium. The p side is 10 nm thick while the n side is 20 nm.

## II. TJ-BAND DIAGRAM, MODELED CHARACTERISTICS, AND EXPERIMENTAL CHARACTERISTICS

Fig. 1 illustrates the energy-band diagram for an AlInAs–InP TJ doped  $2 \times 10^{20} \text{ cm}^{-3}$  on the p-side and  $5 \times 10^{19} \text{ cm}^{-3}$  on the n-side. This particular configuration benefits from a Type-II band alignment which facilitates the degeneracy necessary for TJ operation. The fundamental tunneling current is given by [15]

$$I \equiv A \int [F_c(E) - F_v(E)]^* G_c(E) * G_v(E) * z^* de \quad (1)$$

where  $F_c(E)$  and  $F_v(E)$  are the Fermi probability functions in the conduction and valence bands, respectively,  $G_c(E)$  and  $G_v(E)$  are the density of states functions in the conduction and valence bands, respectively, and  $z$  is the tunneling probability. Fig. 1 demonstrates that the stated doping levels place the Fermi level significantly further into the conduction band of the n++ side than the valence band of the p++ side. Since changes in Fermi level will more significantly affect the number of available states in the valence band as opposed to the conduction band, acceptor concentration gradients will predominantly determine the current–voltage ( $I$ – $V$ ) characteristics of the diode.

A closed-form solution to (1) is given by

$$J \equiv J_p \left( \frac{V}{V_p} \right) \exp \left( 1 - \frac{V}{V_p} \right) \quad (2)$$

where  $J_p$  and  $V_p$  are the current density and voltage values corresponding to the peak tunneling current density before the Esaki dip [16].  $J_p$  and  $V_p$  have been analytically defined by Demassa *et al.* as [15]

$$V_p \approx \frac{(V_n + V_p)}{3} \quad (3)$$

and

$$J_p = \frac{qm^*}{36h^3} E_{\perp} D \exp \left[ \frac{\pi m^{*1/2} E_g^{3/2}}{2(2)^{1/2} h F} \right]$$

where

$$E_{\perp} = \frac{2^{1/2} h F}{\pi m^{*1/2} E_g^{1/2}}$$

$$F = \left( \frac{q^3}{2\epsilon} \right)^{1/2} n^{*1/2} V_d^{1/2} \quad (4)$$

where  $V_n$  and  $V_p$  represent the degree of Fermi-level penetration into the conduction and valence bands on the n and p sides, respectively,  $m^*$  is the reduced effective mass,  $D$  is the overlap integral and can be estimated as  $V_P$ , and  $V_d$  serves as the diffusion potential estimated by  $E_g$ . For simplicity, we assume a homojunction model in our calculations. The staggered lineup of AlInAs–InP TJs simply reduces the diffusion potential and the estimations serve as a worst-case scenario.

We can use (3) and (4) to generate theoretical  $J$ – $V$  characteristics for TJs based on doping and bandgap variations and subsequently fit these characteristics to experimental results to deduce the actual doping density of our test structures and devices. Fig. 2 shows  $J$ – $V$  characteristics at various bandgap energies for TJs with the expected doping levels mentioned earlier in this section. According to the data, we should observe a negligible 25-mV voltage drop across our AlInAs–InP TJ at a nominal operating current density of  $10 \text{ kA/cm}^2$  and reduce the drop even further by using a 1.2Q AlInGaAs–AlInGaAs TJ. The 1.3Q and 1.4Q TJs are instructive for  $1.55\text{--}\mu\text{m}$  device design but will severely limit performance in  $1.3\text{-}\mu\text{m}$  devices due to band-to-band optical absorption. Groups have seen operating voltage drops on the order of 30 mV in InGaAs-based TJs [17]. The 25-mV voltage drop corresponds to an effective contact resistivity of  $2.5 \times 10^{-6} \Omega\text{-cm}^2$ , similar to the best p-type contact resistivities and generally accepted n-type contact resistivities [18], [19].

No group developing Al-based TJs for LW-VCSELs has reportedly seen characteristics on par with the values observed in Fig. 2. Our best TJ test structures produce results represented in Fig. 3, with a contact resistivity an order of magnitude larger than the calculated characteristic results ( $\sim 2.5 \times 10^{-5} \Omega\text{-cm}^2$ ). We display the entire forward and reverse bias sweep of the experimental TJ in Fig. 4 to confirm tunneling operation in our devices. We use the peak current density and voltage in all the modeling presented in this work. Fig. 5 shows calculated TJ characteristics more consistent with our VCSEL TJ characteristics. Based on the model, our best test structures show approximate acceptor doping levels of  $1 \times 10^{19} \text{ cm}^{-3}$ , which is an order of magnitude lower than the designed value. Fig. 5 also shows the impact of  $1 \times 10^{18} \text{ cm}^{-3}$  changes in acceptor doping levels. Equal changes in donor doping levels yield minimal changes in  $J$ – $V$  characteristics.

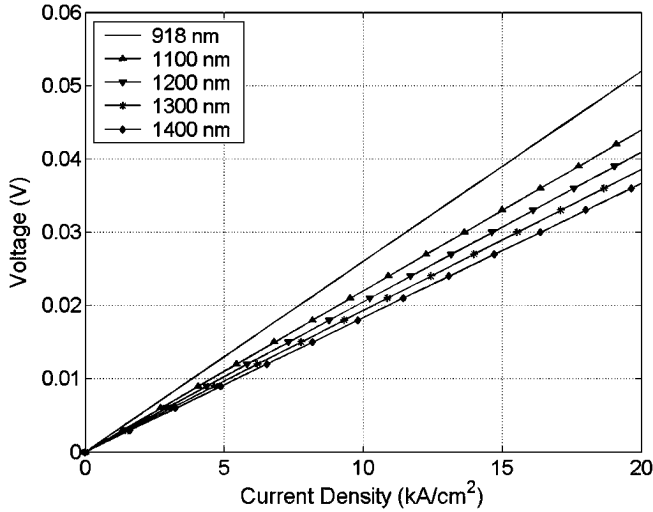


Fig. 2. Calculated variation in characteristics for various band gap TJ characteristics at nominal VCSEL operating current densities (10–20 kA/cm<sup>2</sup>). Calculations assume  $2 \times 10^{20} \text{ cm}^{-3}$  and  $5 \times 10^{19} \text{ cm}^{-3}$  on the p and n sides, respectively. Recall that the n++ layer thickness is 20 nm and the p++ layer thickness is 10 nm.

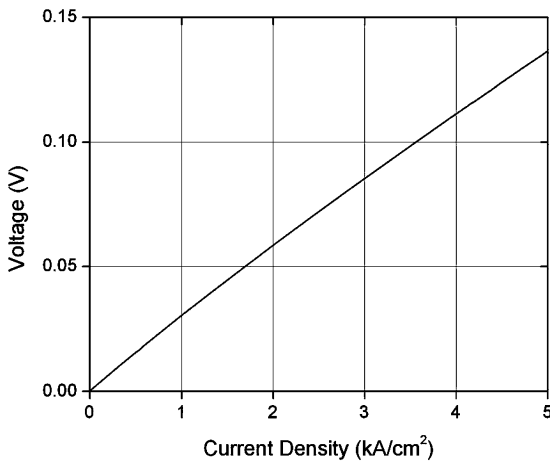


Fig. 3. Measured data for best TJ test structures. Only the reverse bias characteristics are shown to emulate VCSEL  $I$ - $V$  characteristics.

Several tunnel diode device structures, such as metal–insulator–semiconductor (MIS) devices, take advantage of two-step tunneling associated with deep-level interfacial defects to assist in the tunneling process [20], [21]. Impurities such as Sb at the n++/p++ interface could have the same effect on the TJs examined in this study and, in the process, reduce the absolute resistance of the TJ. Since none of our measured TJs include intentional interfacial impurities, we do not consider the effect of these defects in the modeling of the TJ. Moreover, the mature growth technology associated with the InP-based TJs examined in this work and the onset of tunneling at the origin of the  $I$ - $V$  curve lead us to believe that the structure acts as a standard TJ. That being said, we would like to note that further improvements could potentially be made to our TJ through the incorporation of deep level defects at the tunneling interface such as Sb. As a final comment in regards to tunneling mechanisms, we refer to the onset of tunneling at the origin of the  $I$ - $V$  curve for the

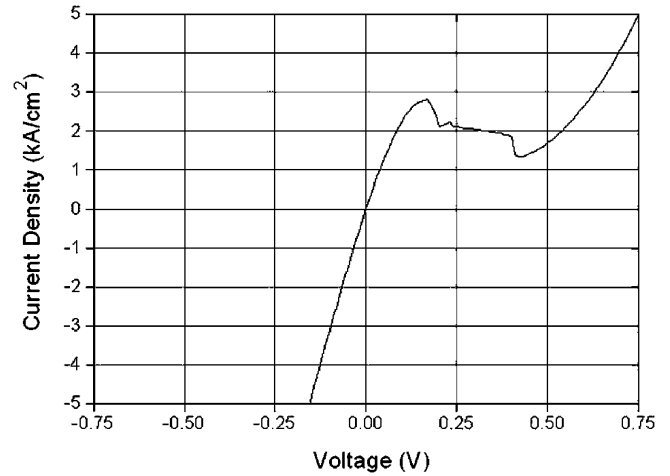


Fig. 4. Forward and reverse bias characteristics of TJ test structure in Fig. 4. Tunneling characteristics are confirmed in quadrant I.

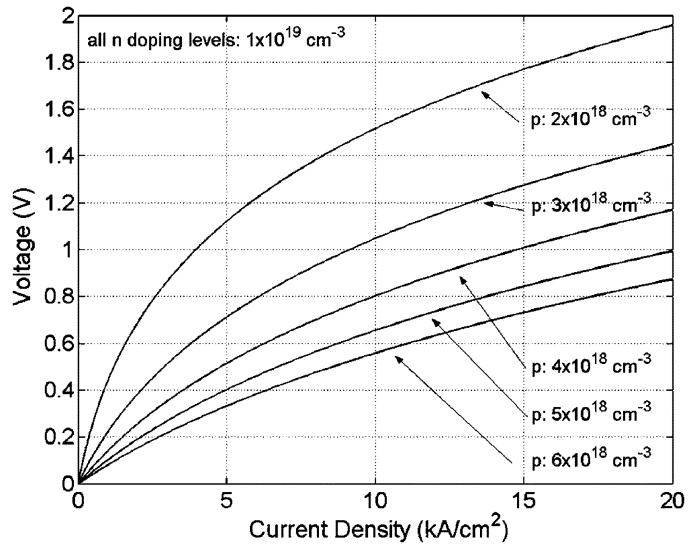


Fig. 5. Calculated  $J$ - $V$  curves for TJ structures with lower doping levels than Fig. 2. These curves more closely resemble the experimental data in Fig. 3. The curve shows the large effect of p-doping variation on TJ characteristics. All curves assume n-type doping of  $1 \times 10^{19} \text{ cm}^{-3}$  and vary p-type doping from  $2 \times 10^{18}$  to  $6 \times 10^{18} \text{ cm}^{-3}$ .

experimental TJ characteristics in Fig. 4. TJ degradation mechanisms involving saturation would manifest themselves as a delay in the reverse bias turn-on characteristics that are not seen in the experimental data.

Actual LW-VCSELS show voltages with even higher extracted resistivities than our best test structures, as will be shown in Section V. Possible reasons for low acceptor levels include nonoptimized C–In and III–V ratios during the epitaxial deposition process and increased dopant diffusion or compensation during growth of the VCSEL structure versus the Hall samples [14]. Furthermore, the electric field gradient will vary for the actual sample when compared with the Hall samples due to the absence of the alternate highly doped layer of the TJ in the Hall sample, presenting another factor which could serve to displace acceptor ions from their primary lattice sites.

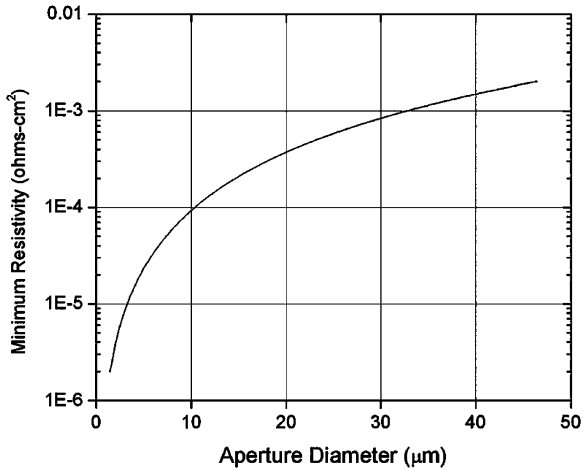


Fig. 6. Minimum TJ resistivity allowed to uniformly spread carriers throughout various diameter TJ aperture.

### III. LATERAL CURRENT-SPREADING OPTIMIZATION

Given an intracavity contacting scheme, a simple analytic expression to define the current density as a function of distance from the aperture edge is given by [22]

$$J = \frac{V_o}{R_{td}} \exp\left(\frac{x}{\xi}\right), \quad \xi = \sqrt{l_h^* \sigma_h^* R_{td}} \quad (5)$$

where  $x$  is the distance from the aperture edge,  $R_{td}$  is the TJ resistivity,  $l_h$  is the contact layer thickness,  $\sigma_h$  is the contact layer conductivity, and  $\xi$  defines a characteristic length which we will use to determine the optimal resistivity of the current spreading TJ aperture.

In order to realize SM VCSEL operation, the current must spread evenly throughout the TJ aperture. Previous work has shown that, in order for the highly resistive layer to provide uniform current spreading,  $\xi$  should be larger than the radius of the current-confining aperture [22]. We hold  $l_h$  and  $\sigma_h$  constant at values which optimize the optical loss/resistance tradeoff from the contact layer. Fig. 6 plots characteristic length versus resistivity for our given structural and material parameters and denotes the minimum resistivity necessary to evenly spread carriers in apertures of between 8–20  $\mu\text{m}$ . Any reduction in resistivity from these values will cause current crowding around the edges of the TJ aperture and enhanced MM VCSEL operation. Our VCSEL results corroborate this model as we see more output power in higher order lasing modes rather than the fundamental mode on devices between 12–20  $\mu\text{m}$  [6]. Devices with 8- $\mu\text{m}$  apertures show SM operation and, concurrently, more uniform current distribution. According to Fig. 6, the resistivity threshold for uniform pumping on an 8- $\mu\text{m}$  aperture is  $6 \times 10^{-5} \Omega\text{-cm}^2$ . While this is a bit higher than our best test structure results, the value is less than what we see in actual devices. Table I shows the p-doping values which correspond to the SM threshold for both 918- and 1200-nm bandgap TJs. We note several observations when considering the data from Fig. 6 and Table I. First, a highly conductive TJ is not the best design for optimized SM performance unless the structure includes an alternate high-mobility layer to spread the carriers uniformly.

TABLE I  
MAXIMUM ALLOWED TJ DOPING LEVELS WHICH WILL SPREAD CARRIERS UNIFORMLY THROUGHOUT THE APERTURE FOR 8-, 12-, 16-, AND 20- $\mu\text{m}$  DEVICES. THEY CAN ALSO BE THOUGHT OF AS OPTIMIZED DOPING LEVELS FOR SM DEVICE DESIGN

Aperture size (in $\mu\text{m}$ )	Optimized p-doping @ $E_g=918 \text{ nm}$	Optimized p-doping @ $E_g=1200 \text{ nm}$
8	$5 \times 10^{18} \text{ cm}^{-3}$	$2.3 \times 10^{18} \text{ cm}^{-3}$
12	$3 \times 10^{18} \text{ cm}^{-3}$	$1.5 \times 10^{18} \text{ cm}^{-3}$
16	$2 \times 10^{18} \text{ cm}^{-3}$	$1.1 \times 10^{18} \text{ cm}^{-3}$
20	$1 \times 10^{18} \text{ cm}^{-3}$	$1 \times 10^{18} \text{ cm}^{-3}$

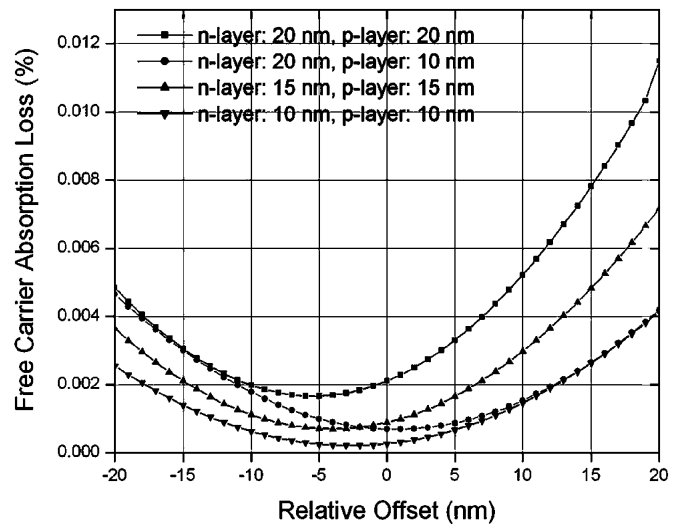


Fig. 7. Free-carrier absorption (FCA) versus relative offset of the n++/p++ TJ interface from a standing wave null. The structure assumes doping levels of  $2 \times 10^{18} \text{ cm}^{-3}$  and  $10 \times 10^{18} \text{ cm}^{-3}$  on the p-side and n-side, respectively. The four curves show the loss characteristics for various TJ dimensions. All TJ dimensions illustrated will allow for proper TJ operation.

Second, large devices for use in high-power multimode applications may be better suited for use with current pumping through a DBR which naturally spreads carriers more evenly throughout an aperture than intracavity schemes. However, a highly reflective, highly conductive, and low-loss epitaxial DBR has been difficult to achieve for 1310-nm emitting devices. Solutions such as wafer-bonded devices incorporating conduction through the DBR add an extra voltage component through the bonded interface, and the use of dielectric or metamorphic DBRs eliminates any opportunity to pump current through the DBRs. Therefore, in the case of SM devices, where output power is typically lower, the added free carrier absorption loss and the voltage drops associated with these DBR schemes may limit the benefits of current conduction through the DBR.

### IV. WKB PARAMETER AND TUNNELING PROBABILITY

Before calculating the complete device  $I$ - $V$  and  $L$ - $I$  characteristics, we define the physical limits of tunneling in order

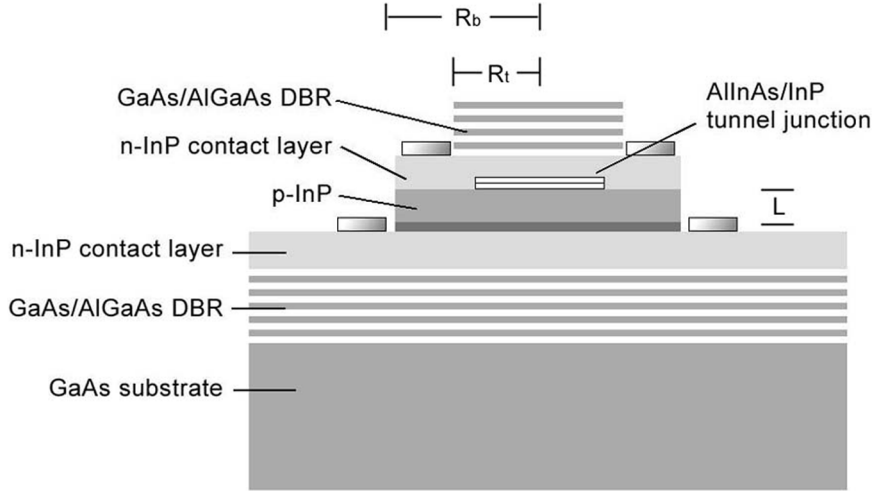


Fig. 8. Basic device structure.  $R_b$  represents the bottom contact inner radius and  $R_t$  represents the top contact inner radius. These two dimensions define the lateral spreading resistance associated with the intra-cavity contacts.  $L$  defines the length of the p-cladding layer.

to minimize optical loss using a metric coined by Mars *et al.*, which is the WKB parameter [13]

$$\text{WKB} \cong 2 \int_{x_1}^{x_2} \sqrt{\frac{2m^*}{\hbar^2}(E_c - E_f)} dx. \quad (6)$$

As WKB increases linearly, the tunneling probability  $\approx$  decreases exponentially. The relationship between these parameters can be found elsewhere [13]. The limits of integration  $x_1$  and  $x_2$  are delineated in Fig. 1 and serve as the constructs for the quantum tunneling width. The energy potential barrier is defined as  $(E_c - E_f)$  and closely resembles a triangular potential barrier with an energy barrier defined by  $(E_g/2 - q\epsilon x)$ , where  $E_g$  and  $\epsilon$  define the bandgap and electric field, respectively.

The WKB parameter serves as a first-order design metric in determining TJ-layer thickness. The TJ needs to be thick enough so as not to deplete the layers, but as thin as possible to minimize free-carrier optical absorption. Fig. 7 displays the single-pass absorption due to free-carrier losses in the TJ versus the relative offset of the TJ layer from a standing wave null for three-layer thickness variations. We calculate free carrier absorption loss coefficients of  $65 \text{ cm}^{-1}$  for the p++ side and  $20 \text{ cm}^{-1}$  for the n++ side for the optimized doping levels on an  $8\text{-}\mu\text{m}$  aperture, which is the most likely to provide SM operation, calculated in the previous section [23]. The corresponding optimized doping levels are  $5 \times 10^{18} \text{ cm}^{-3}$  and  $1 \times 10^{19} \text{ cm}^{-3}$  on the p-side and n-side, respectively, corresponding to absorption coefficient values of  $13 \text{ cm}^{-1}$  per  $1 \times 10^{18} \text{ cm}^{-3}$  and  $2.0 \text{ cm}^{-1}$  per  $1 \times 10^{18} \text{ cm}^{-3}$ , respectively. Zero offset corresponds to the n-p interface placed at a standing wave null. A positive relative offset represents the TJ moving towards the active region of the device. The 20-nm n-layer and the 10-nm p-layer serve as our default test structure values. We can reduce the n-layer thickness from 20 to 10 nm and minimize absorption without any increase in the WKB parameter. We can reduce the n- and p-layer thicknesses even further, but we then begin to see an increase in the WKB parameter and orders-of-magnitude reduction in tunneling probability. The greatest advantage gained from reducing

layer thickness and optical loss is improved growth tolerances. We observe an order-of-magnitude increase in loss from growth aberrations on the order of tens of nanometers as we increase the 10-nm TJ layers to 20 nm.

#### V. VOLTAGE CONTRIBUTION OF OTHER SOURCES IN AN INTRACAVITY CONTACTED VCSEL STRUCTURE

Now that we have theoretically designed the TJ to operate at the lowest possible voltage while still facilitating SM VCSEL requirements, we can incorporate the remaining voltage contributors into a complete electrical model for the device. Fig. 8 shows our complete VCSEL structure.  $R_t$  represents the distance from the top contact to the center of the TJ,  $R_b$  represents the distance from the lower contact to the center of the TJ, and  $L$  represents the thickness of the p-cladding layer. The active region diode, intracavity contact related resistances associated with electron transport from the TJ to the top contact, the bottom contact to the active region, p-cladding layer resistances, and other heterobarrier voltages will also contribute significantly to the overall  $I$ - $V$  characteristics of these devices.

The fundamental equation governing the n-contact layer lateral spreading resistance is given by [24]

$$R_{\text{sp}} = \frac{\rho_n}{2L\pi} \ln \left( \frac{R_{t,b}}{R_a} \right) \quad (7)$$

where  $\rho_n$  represents the n-type layer resistivity,  $R_{t,b}$  corresponds to either the top or bottom inner contact radius, and  $R_a$  refers to the TJ aperture radius. We calculate the resistance associated with p-cladding layer vertical transport using the basic equation  $R = \rho_p L/A$ , where  $A$  represents the cross-sectional area and  $\rho_p$  corresponds to the p-type cladding layer resistivity. Modeled voltage contributions from each of these, given the geometries and thicknesses associated with our experimental structure, are plotted in Fig. 9 for an  $8\text{-}\mu\text{m}$  TJ aperture. The experimental structure incorporates a  $25\text{-}\mu\text{m}$  top inner contact radius and a  $46 \mu\text{m}$  bottom inner contact radius. The values for  $\rho_n$  and  $\rho_p$  are  $3.8 \times 10^{-3} \Omega\text{-cm}$  and  $0.4 \Omega\text{-cm}$ , respectively, based on InP n- and p-type doping levels of  $1 \times 10^{18} \text{ cm}^{-3}$  and

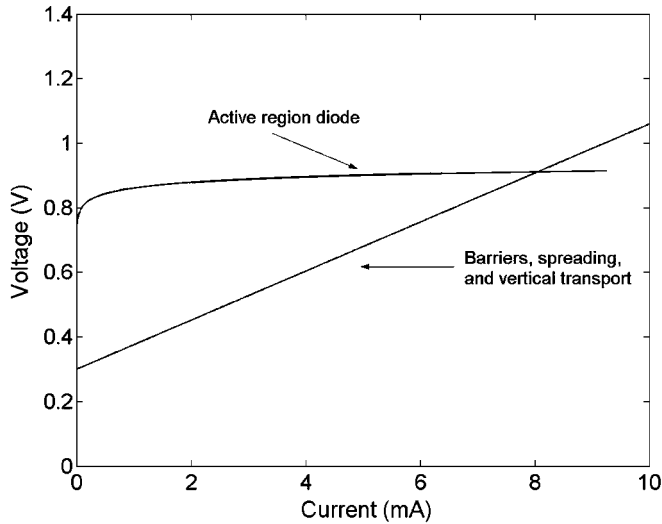


Fig. 9.  $I$ - $V$  characteristics of voltage contributions other than the TJ. We include the active region diode characteristic, lateral spreading resistance, vertical transport resistance, and barrier voltage. Device dimensions are 25 and 46  $\mu\text{m}$  for  $R_t$  and  $R_b$ , respectively, and a 400-nm p-cladding layer.

TABLE II  
VARIOUS RESISTANCE CONTRIBUTIONS FOR THE FIRST-GENERATION  
EXPERIMENTAL STRUCTURE VERSUS THE OPTIMIZED DIMENSIONS OF:  
 $R_t = 12 \mu\text{m}$ ,  $R_b = 25 \mu\text{m}$ , AND  $L = 200 \text{ nm}$

	Top Contact Spreading Resistance ( $\Omega$ )	Bottom Contact Spreading Resistance ( $\Omega$ )	p-Cladding Resistance ( $\Omega$ )	Hetero-barrier voltage (V)
Experimental Structure	27.1	36.12	32.63	.3
Optimized Structure	16.25	27.1	16.31	0

$5 \times 10^{17} \text{ cm}^{-3}$ , respectively [23]. The 0.3-V built-in voltage is inherent to the ungraded AlInAs-InP interface between the InP n-cladding and the undoped AlInAs active region layer [25].

We now calculate amount by which we can reduce the voltage contribution of the spreading, transport, and barrier layers by reducing device geometries to sizes still within our fabrication capability. We decrease the top inner contact radius from 25 to 12  $\mu\text{m}$ , decrease the bottom inner contact radius from 46 to 25  $\mu\text{m}$ , reduce the p-cladding layer thickness from 400 to 200 nm, which is a reduction from a full-wavelength layer to a half-wavelength layer, and grade the doping around the hetero-barrier to remove the heterointerface voltage. Table II shows the improvement in differential resistance and voltage calculated at 10 mA for an 8- $\mu\text{m}$  aperture for each of these changes. The optimized geometries reduce the initial voltage drop 0.3 V and improve the overall differential resistance by 36.19  $\Omega$ . All differential resistance values are calculated for nominal VCSEL operating current levels, i.e., 10 mA. While the voltage improvement due to geometry optimization is not as large as the improvement afforded through TJ optimization, it is nonetheless important as it nudges the total differential resistance towards 50  $\Omega$ , which is a key parameter for devices intended for use in transmission-line systems.

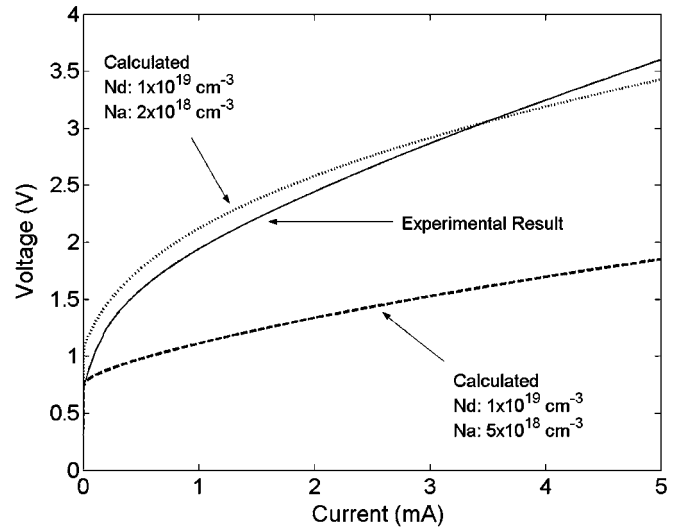


Fig. 10.  $I$ - $V$  characteristics for an 8- $\mu\text{m}$  first-generation device versus calculated curves based on the  $I$ - $V$  characteristics of the TJ and other factors modeled in this chapter. The top calculated curve shows a nice fit with experimental data while the bottom calculated curve shows optimal  $I$ - $V$  characteristics for an 8- $\mu\text{m}$  SM TJ apertured device.

## VI. COMPLETE DEVICE MODEL AND SM DEVICE OPTIMIZATION

Now that we have optimized the entire VCSEL design to minimize the voltage contribution of each resistive element in the device while still maintaining uniform current spreading, we can compare  $I$ - $V$  models for experimental and theoretically optimized devices and predict the improvement in output power associated with the voltage reduction. An experimental  $I$ - $V$  curve for an 8- $\mu\text{m}$  VCSEL is plotted in Fig. 10 along with two calculated curves. All calculated curves assume an 8- $\mu\text{m}$  aperture. The calculated curve which is in strong agreement with the experimental curve is derived using structural and material values equal to those in the experimental structure, which includes an 8- $\mu\text{m}$ -diameter aperture, a 400-nm-thick n-contact layer, and a 400-nm-thick p-contact layer. In order for the curves to closely match, we must reduce the actual acceptor concentration in the p++ AlInAs layer of the TJ to  $1.7 \times 10^{18} \text{ cm}^{-3}$ . As mentioned in Section II, the overestimated acceptor concentration can arise from many factors, most of which cause large portions of the C content to act as donors rather than acceptors. Low-temperature AlInAs growth as well as C-In ratio and III-V ratio optimization should improve the acceptor concentration in the p++ layers. Other groups developing TJs for use in 1300-nm VCSELs have demonstrated low-voltage devices and confirm that higher acceptor concentrations are possible, although, to the best of our knowledge, none of these groups have designed TJs to optimize SM characteristics.

The maximum acceptor concentration for SM operation as defined by Table I is  $5 \times 10^{18} \text{ cm}^{-3}$  for an 8- $\mu\text{m}$  device. The second calculated curve in Fig. 10 is a result of combining a TJ with an optimized acceptor concentration and the new device geometries stated in the previous section. This curve presents the optimized  $I$ - $V$  characteristics for an 8- $\mu\text{m}$  device. The optimization process reduces the differential resistance from

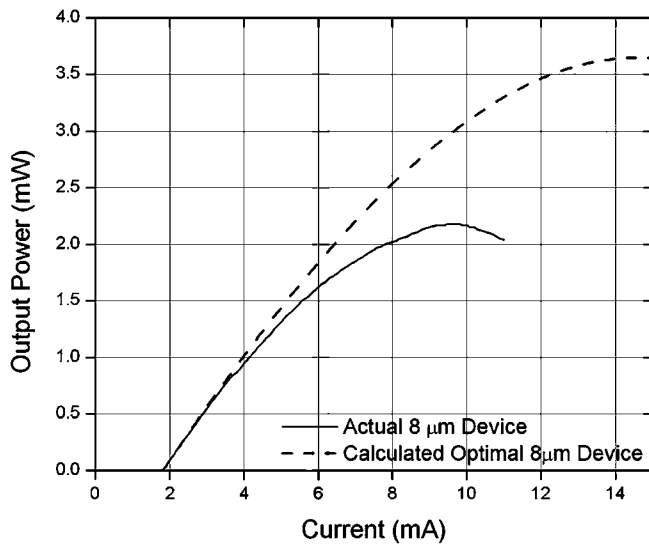


Fig. 11. Perceived improvement in output power through electrical optimization. The calculations are made for an 8- $\mu\text{m}$  aperture diameter at 20  $^{\circ}\text{C}$ .

300 to 150  $\Omega$  and allows the devices to operate well under 3 V, which is an important metric in LW-VCSEL design, since most devices are driven by 3.3-V electrical driver circuitry. Given the theoretical improvement in  $I$ - $V$  characteristics, we can estimate the potential improvement in output power of the VCSEL, as demonstrated in Fig. 11. We expect the output power to roll over at higher current levels than in the experimental curve due to a slower rate of heating in the active region. The reduction in active region temperature will increase the gain at a given current level. Driving the device at higher current densities will allow excess carriers to contribute directly to stimulated emission and improve the output power of the device. Given a thermal impedance value of 1.289  $^{\circ}\text{C}/\text{mW}$  and the  $LIV$  characteristics recorded previously [6], we can derive a junction temperature–differential efficiency relationship. We can then apply this relationship to a device exhibiting the optimized  $I$ - $V$  characteristics from Fig. 10 in order to predict the differential efficiency at a given current. Using this optimized device design, we see a 1.5-mW increase in output power, which is a significant improvement.

By improving the  $I$ - $V$  characteristics, we not only increase the absolute output power, but we also increase the roll-over current of the device. Because the resonance frequency of diode lasers is inherently based on the difference between the drive and threshold currents, increasing the roll-over current will also serve to increase the modulation bandwidth.

## VII. SUMMARY

We present a methodology for TJ design and incorporation in SM LW-VCSELS. Using band diagrams and the WKB approximation, we determine the TJ layer thicknesses which optimize tunneling probability and optical loss due to the TJ. We find that our present 20-nm n++-InP layer can be reduced to 10 nm without any loss of tunneling probability.

Once we determine the physical dimensions of the TJ, we examine the effects of varying the doping levels from our expected levels of  $5 \times 10^{19} \text{ cm}^{-3}$  on the n-side and  $2 \times 10^{20} \text{ cm}^{-3}$  on the

p-side and attempt to match experimental TJ results with calculated curves. While it is evident from inspection that our experimental results do not resemble characteristics of highly degenerate TJs, we quantify the discrepancy as an order of magnitude reduction in acceptor concentration on the p++ side of the TJ. Variations in donor concentration do not prove to have much effect on the operation of InP-based TJs.

While our designed doping levels would yield low voltage devices, the TJs would not support single-mode operation of VCSELS. An 8- $\mu\text{m}$  aperture requires a minimum resistivity of  $6 \times 10^{-5} \Omega\text{-cm}^2$  to uniformly inject current into the active region. This resistivity corresponds to an acceptor concentration of  $5 \times 10^{18} \text{ cm}^{-3}$ , which is more than an order of magnitude less than our design levels. Given this optimized resistivity and doping level, we calculate the  $I$ - $V$  and  $L$ - $I$  characteristics for an optimized 8- $\mu\text{m}$  device and predict devices operating well under 3 V and SM output powers exceeding 3.5 mW.

## REFERENCES

- [1] O. Boriclubeecke, D. S. Pan, and T. Itoh, "Fundamental and subharmonic excitation for an oscillator with several tunneling diodes in series," *IEEE Trans. Microw. Theory Tech.*, vol. 43, no. 4, pp. 969–976, Apr. 1995.
- [2] O. Kwon, M. M. Jazwiecki, R. N. Sacks, and S. A. Ringel, "High-performance, metamorphic  $\text{In}_x\text{Ga}_{1-x}\text{As}$  tunnel diodes grown by molecular beam epitaxy," *IEEE Electron Device Lett.*, vol. 24, no. 10, pp. 613–615, Oct. 2003.
- [3] L. Esaki, "New phenomenon in narrow germanium para-normal-junctions," *Phys. Rev.*, vol. 109, pp. 603–604, 1958.
- [4] D. I. Babic, J. Piprek, K. Streubel, R. P. Mirin, N. M. Margalit, D. E. Mars, J. E. Bowers, and E. L. Hu, "Design and analysis of double-fused 1.55- $\mu\text{m}$  vertical-cavity lasers," *IEEE J. Quantum Electron.*, vol. 33, no. 8, pp. 1369–1383, Aug. 1997.
- [5] M. Ortsiefer, S. Baydar, K. Windhorn, G. Bohm, J. Roskopf, R. Shau, E. Ronneberg, W. Hofmann, and M. C. Amann, "2.5-mW single-mode operation of 1.55- $\mu\text{m}$  buried tunnel junction VCSELS," *IEEE Photon. Technol. Lett.*, vol. 17, no. 8, pp. 1596–1598, Aug. 2005.
- [6] V. Jayaraman, M. Mehta, A. W. Jackson, S. Wu, Y. Okuno, J. Piprek, and J. E. Bowers, "High-power 1320-nm wafer-bonded VCSELS with tunnel junctions," *IEEE Photon. Technol. Lett.*, vol. 15, no. 11, pp. 1495–1497, Nov. 2003.
- [7] J. Cheng, C.-L. Shieh, X. Huang, G. Liu, M. V. R. Murty, C. C. Lin, and D. X. Xu, "Efficient CW lasing and high-speed modulation of 1.3- $\mu\text{m}$  AlGaInAs VCSELS with good high temperature lasing performance," *IEEE Photon. Technol. Lett.*, vol. 17, no. 1, pp. 7–9, Jan. 2005.
- [8] V. Iakovlev, G. Suruceanu, A. Caliman, A. Mereuta, A. Mircea, C. A. Berseth, A. Syrbu, A. Rudra, and E. Kapon, "High-performance single-mode VCSELS in the 1310-nm waveband," *IEEE Photon. Technol. Lett.*, vol. 17, no. 5, pp. 947–949, May 2005.
- [9] D. Feezell, D. Buell, and L. Coldren, "InP-Based 1.3–1.6  $\mu\text{m}$  VCSELS with selectively etched tunnel junction apertures on a wavelength flexible platform," *IEEE Photon. Technol. Lett.*, vol. 17, no. 10, pp. 2017–2019, Oct. 2005.
- [10] D. Feezell, L. Johansson, D. Buell, and L. Coldren, "Efficient modulation of InP-based 1.3  $\mu\text{m}$  VCSELS with AsSb-based DBRs," *IEEE Photon. Technol. Lett.*, vol. 17, no. 11, pp. 2253–2255, Nov. 2005.
- [11] J. Boucart, C. Starck, F. Gaborit, A. Plais, N. Bouche, E. Derouin, J. C. Remy, J. Bonnet-Gamard, L. Goldstein, C. Fortin, D. Carpentier, P. Salet, F. Brillouet, and J. Jacquet, "Metamorphic DBR and tunnel-junction injection. A CW RT monolithic long-wavelength VCSEL," *IEEE J. Sel. Topics Quantum Electron.*, vol. 5, no. 3, pp. 520–521, May-Jun. 1999.
- [12] C. K. Lin, D. P. Bour, J. Zhu, W. H. Perez, M. H. Leary, A. Tandon, S. W. Corzine, and M. R. T. Tan, "High temperature continuous-wave operation of 1.3- and 1.55- $\mu\text{m}$  VCSELS with InP/air-gap DBRs," *IEEE J. Sel. Topics Quantum Electron.*, vol. 9, no. 5, pp. 1415–1421, Sep.–Oct. 2003.
- [13] D. E. Mars, Y. L. Chang, M. H. Leary, S. D. Roh, and D. R. Chamberlin, "Low-resistance tunnel junctions on GaAs substrates using GaInNAs," *Appl. Phys. Lett.*, vol. 84, pp. 2560–2562, 2004.
- [14] J. Yan, G. Ru, Y. Gong, and F. S. Choa, "Study of P-type carbon doping on  $\text{In}_{0.53}\text{Ga}_{0.47}\text{As}$ ,  $\text{In}_{0.52}\text{Al}_{0.2}\text{Ga}_{0.28}\text{As}$  and  $\text{In}_{0.52}\text{Al}_{0.48}\text{As}$ ," *Proc. SPIE*, vol. 5260, *Appl. Photon. Technol.* 6, pp. 446–449, 2003.

- [15] T. A. Demassa and D. P. Knott, "Prediction of tunnel diode voltage-current characteristics," *Solid-State Electron.*, vol. 13, pp. 131–131, 1970.
- [16] S. M. Sze, *Physics of Semiconductor Devices*. New York: Wiley-Interscience, 1969.
- [17] M. Arzberger, M. Lohner, G. Bohm, and M. C. Amann, "Low-resistivity p-side contacts for InP-based devices using buried InGaAs tunnel junction," *Electron. Lett.*, vol. 36, pp. 87–88, 2000.
- [18] M. H. Park, L. C. Wang, J. Y. Cheng, and C. J. Palmstrom, "Low resistance ohmic contact scheme (similar to  $\mu\Omega\text{cm}^{(2)}$ ) to p-InP," *Appl. Phys. Lett.*, vol. 70, pp. 99–101, 1997.
- [19] C. L. Chen, L. J. Mahoney, M. C. Finn, R. C. Brooks, A. Chu, and J. G. Mavroides, "Low resistance Pd/Ge/Au and Ge/Pd/Au Ohmic contacts to normal-type GaAs," *Appl. Phys. Lett.*, vol. 48, pp. 535–537, 1986.
- [20] S. Ahmed, M. R. Melloch, E. S. Harmon, D. T. McInturff, and J. M. Woodall, "Use of nonstoichiometry to form GaAs tunnel junctions," *Appl. Phys. Lett.*, vol. 71, pp. 3667–3669, 1997.
- [21] A. M. Andrews, H. W. Korb, N. Holonyak, Jr, C. B. Duke, and G. G. Kleiman, "Tunnel mechanisms and junction characterization in III–V tunnel diodes," *Phys. Rev. B*, vol. 5, pp. 2273–2295, 1972.
- [22] J. W. Scott, "Design, fabrication and characterization of high-speed intra-cavity contacted vertical-cavity lasers," Ph.D. dissertation, Elect. Comput. Eng. Dept., Univ. California, Santa Barbara, 1995.
- [23] D. I. Babic, "Double-fused long-wavelength vertical-cavity lasers," Ph.D. dissertation, Elect. Comput. Eng. Dept., Univ. California, Santa Barbara, 1995.
- [24] E. M. Hall, "Epitaxial approaches to long-wavelength vertical-cavity lasers," Ph.D. dissertation, Mater. Eng. Dept., Univ. California, Santa Barbara, 2001.
- [25] J. Piprek, V. Jayaraman, M. Mehta, and J. E. Bowers, "Balanced optimization of 1.31  $\mu\text{m}$  tunnel-junction VCSELs," in *Proc. IEEE/LEOS 3rd Int. Conf. Numerical Simulation of Semicond. Optoelectron. Devices*, Piscataway, NJ, pp. 45–6 2003.

**Manish Mehta** received the Ph.D. degree in electrical engineering from the University of California, Santa Barbara, in 2006.

He is currently working on the development of mid-infrared semiconductor lasers as a Post-Doctoral Researcher under Dr. Diana Huffaker with the University of New Mexico, Albuquerque.

**Danny Feezell** received the B.S. degree in electrical engineering from the University of California, Irvine, in 2000, and the M.S. and Ph.D. degrees from the University of California, Santa Barbara, in 2001 and 2005, respectively.

He is currently working on design, fabrication, and characterization of novel GaN-based light-emitting devices as a Post-Doctoral Researcher under Prof. Shuji Nakamura with the University of California, Santa Barbara.

**David A. Buell** received the Ph.D. degree in materials from the University of California, Santa Barbara, in 2005. His doctoral work focused on InP-based vertical cavity lasers.

He is a researcher of molecular beam epitaxy of III–V and II–IV semiconductors with a focus on optoelectronics and optical phenomena. He is currently researching ZnO at CNRS-CRHEA as a Chateaubriand Fellow.

**Andrew W. Jackson** received the B.A. degree in physics from Princeton University, Princeton, NJ, in 1994, and the Ph.D. degree in materials engineering from the University of California, Santa Barbara, in 1999.

From 1999 to 2002, he worked at Cielo Communications developing the first commercial InGaAsN-based 1.3- $\mu\text{m}$  VCSELs. Since 2003, he has been a Project Scientist with the Electrical and Computer Engineering Department, University of California, Santa Barbara. His research interests are currently focused on materials growth by molecular beam epitaxy. He is the author or coauthor of 30 technical papers and holds seven U.S. patents.

**Larry A. Coldren** (S'67–M'72–SM'77–F'82) received the Ph.D. degree in electrical engineering from Stanford University, Stanford, CA, in 1972.

After 13 years in the research area at Bell Laboratories, he was appointed Professor of Electrical and Computer Engineering at the University of California at Santa Barbara (UCSB) campus in 1984. In 1986, he assumed a joint appointment with Materials and ECE, and in 2000 the Fred Kavli Chair in Optoelectronics and Sensors. He is also Chairman and Chief Technology Officer of Agility Communications, Inc. At UCSB, his efforts have included work on novel guided-wave and vertical-cavity modulators and lasers as well as the underlying materials growth and fabrication technology. He is now investigating the integration of various optoelectronic devices, including optical amplifiers and modulators, tunable lasers, wavelength-converters, and surface-emitting lasers. He has authored or coauthored over 500 papers, five book chapters, one textbook, and has been issued 32 patents.

Prof. Coldren is a Fellow of the Optical Society of America (OSA) and a past Vice-President of IEEE Laser and Electro-Optics Society (LEOS).

He is the Fred Kavli Professor of Optoelectronics and Sensors at the University of California, Santa Barbara, CA. He is also Chairman and Chief Scientist of Agility Communications, Inc. He received the Ph.D. degree in Electrical Engineering from Stanford University in 1972. After 13 years in the research area at Bell Laboratories, he joined UC-Santa Barbara in 1984 where he now holds appointments in Materials and Electrical & Computer Engineering, and is Director of the Optoelectronics Technology Center. In 1990 he co-founded Optical Concepts, later acquired as Gore Photonics, to develop novel VCSEL technology; and in 1998 he co-founded Agility Communications to develop widely-tunable integrated transmitters.

**John E. Bowers** (S'78–M'81–SM'85–F'93) received the M.S. and Ph.D. degrees from Stanford University, Stanford, CA.

He is the Director of the Multidisciplinary Optical Switching Technology Center (MOST) and a Professor with the Department of Electrical Engineering, University of California, Santa Barbara (UCSB). His research interests are primarily concerned with optoelectronic devices and optical networking. He is a cofounder of the Center for Entrepreneurship and Engineering Management and a cofounder of Terabit Technology and Calient Networks. He worked for AT&T Bell Laboratories and Honeywell before joining UCSB. He has published six book chapters, 350 journal papers, and 600 conference papers and holds 38 patents.

Prof. Bowers is a Fellow of the Optical Society of America and the American Physical Society. He was a recipient of the IEEE LEOS William Streifer Award and the South Coast Business and Technology Entrepreneur of the Year Award.